ACS APPLIED MATERIALS & INTERFACES

Research Article

www.acsami.org

Nanoscale Pillar-Enhanced Tribological Surfaces as Antifouling Membranes

Wansuk Choi,[†,▽] Edwin P. Chan,[‡,▽] Jong-Hyun Park,[§,▽] Won-Gi Ahn,[†] Hyun Wook Jung,[†] Seungkwan Hong,[∥] Jong Suk Lee,[⊥] Ji-Young Han,[#] Sangpil Park,[#] Doo-Hyun Ko,[*,#] and Jung-Hyun Lee[*,†]

[†]Department of Chemical and Biological Engineering, Korea University, 5-1 Anam-dong, Seongbuk-gu, Seoul 136-713, Republic of Korea

[‡]Materials Science and Engineering Division, The National Institute of Standards and Technology (NIST), 100 Bureau Drive, Gaithersburg, Maryland 20899, United States

[§]Department of Chemistry, Korea University, 5-1 Anam-dong, Seongbuk-gu, Seoul 136-713, Republic of Korea

[∥]School of Civil, Environmental and Architectural Engineering, Korea University, 5-1 Anam-dong, Seongbuk-gu, Seoul 136-713, Republic of Korea

[⊥]Department of Chemical and Biomolecular Engineering, Sogang University, 35 Baekbeom-ro, Mapo-gu, Seoul 04107, Republic of Korea

[#]Department of Applied Chemistry, Kyung Hee University, 1732 Deogyeong-daero, Giheung-gu, Yongin-si, Gyeonggi-do 17104, Republic of Korea

Supporting Information

ABSTRACT: We present a nonconventional membrane surface modification approach that utilizes surface topography to manipulate the tribology of foulant accumulation on water desalination membranes via imprinting of submicron titanium dioxide (TiO_2) pillar patterns onto the molecularly structured, flat membrane surface. This versatile approach overcomes the constraint of the conventional approach relying on interfacial polymerization that inevitably leads to the formation of ill-defined surface topography. Compared to the nonpatterned membranes, the patterned membranes showed significantly improved fouling resistance for both organic protein and bacterial foulants. The use of hydrophilic TiO_2 as a pattern material increases the membrane hydrophilicity, imparting improved chemical antifouling resistance to the membrane. Fouling behavior was also interpreted in terms of the topographical effect depending on the relative size of foulants to the pattern dimension. In addition, computational fluid dynamics simulation suggests that the enhanced antifouling of the patterned membrane is attributed to the enhancement in overall and local shear stress at the fluid−TiO_2 pattern interface.

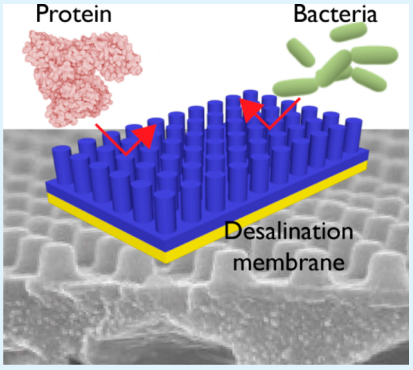

KEYWORDS: *nanoscale patterns, layer-by-layer assembly, antifouling, membranes, thin film composites, water desalination, reverse osmosis*

INTRODUCTION

A myriad of strategies have been explored to reduce or control the fouling of membranes used in desalination and water treatment applications. Although alteration of membrane materials and incorporation of additives or functional nanomaterials have been attempted to mitigate the membrane fouling,[1−4] surface modification methods have been predominantly developed.[5] Generally speaking, these surface modifications can be categorized into two primary strategies. The first approach involves chemically modifying the membrane surface via grafting, adsorption, or coating of functional moieties to reduce the interactions between the foulant and the membrane surface by increasing membrane hydrophilicity and/or controlling its surface charge.[5−7] The second one draws inspiration from organisms found in nature, which is via the advantageous utilization of surface topography to prevent fouling.[8] Recent results have demonstrated that controlled surface topography can indeed reduce foulant−surface interactions and thus mitigate fouling.[9,10] For example, the shark-skin-inspired Sharklet AF patterns have effectively delayed the cell attachment and subsequent biofilm formation compared to a flat surface.[11] Patterned surfaces with micron and submicron topographical features including pillars, lines,

Received: August 29, 2016
Accepted: October 24, 2016
Published: October 24, 2016

DOI: 10.1021/acsami.6b10875
ACS Appl. Mater. Interfaces 2016, 8, 31433−31441

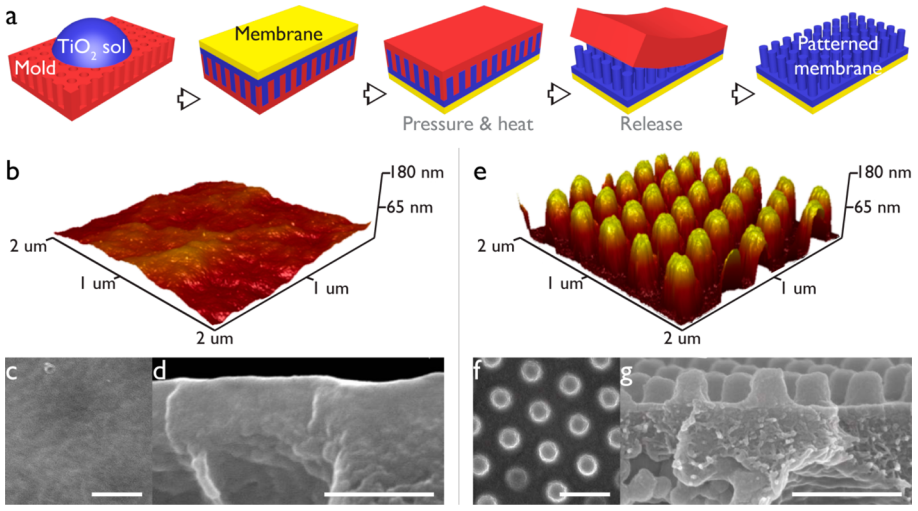

Figure 1. (a) Schematic illustration of the fabrication of the submicron TiO_2-patterned membrane. (b) AFM image of the molecular layer-by-layer (mLbL)-assembled membrane. (c, d) Top-down and cross-sectional SEM images of the mLbL-assembled membrane. (e) AFM image of the TiO_2-patterned membrane. (f, g) Top-down and cross-sectional SEM images of the TiO_2-patterned membrane. Scale bar = 500 nm for all SEM images.

and lamella showed similar promise for preventing organic fouling and biofouling.[9−12]

Inspired by these topographic patterns, membrane scientists have applied a similar concept to the design of antifouling membranes. Innovative methods such as soft-lithographic phase inversion and nanoimprint lithography have been shown to be viable means to construct microscale and nanoscale patterned surfaces on porous microfiltration (MF) and ultrafiltration (UF) membranes.[13−16] For examples, Won et al. created microscale prisms[16−19] and pyramid[16] patterns on porous MF membranes, which led to the reduction of microbial and colloidal fouling. Maruf and co-workers also prepared submicron line-patterned UF membranes to significantly reduce deposition of colloidal particles and protein.[14,20,21] However, the previous membrane patterning technologies have several issues that remain to be addressed. From a practical aspect, most previous works on patterned membranes have been limited to porous MF and UF membranes used for large solute filtration and not molecular filtration such as dense reverse osmosis (RO). Furthermore, relatively simple and anisotropic patterns like lines and prisms have been predominantly explored for developing fouling-resistant patterned membranes and elucidating their antifouling mechanisms, limiting the versatile application of the topographical modification. Importantly, from the fundamental aspect, internal fouling coupled with external fouling for the porous membranes hampered our clear understanding of the true topographical effect on the fouling. These considerations fuel the demand for the study of surface patterning for dense RO desalination membranes whose surfaces were topographically modified with advanced pattern features. Unfortunately, a very limited attempt to control the topography of RO membranes, which typically consist of an ultrathin polyamide (PA) selective layer on a porous UF support, has been made due to the technical challenges arising from the high fragility and intrinsically rough and nonconformal growth mechanism of their PA selective layers prepared via conventional interfacial polymerization (IP). A pioneering work has been done by Maruf et al., who demonstrated the surface patterning of RO membranes with submicron line patterns by forming the PA layer via IP on top of the previously line-patterned UF support membranes.[22,23] However, nonconformal growth and local roughness (like nodular or ridge and valley) of the IP-assembled PA layer on the patterned support remain the critical technical issue to be resolved for creating well-defined and precisely controlled pattern features.[22] In general, there lacks a pragmatic approach for precise controlled patterning that are amenable to the synthesis and fabrication of RO membranes.[22,23]

Here, we report on a new method to fabricate the patterned RO membranes that can overcome the aforementioned constraints imposed on the previous approach. Our strategy relies on the fabrication of a smooth and dense RO membrane via a recently developed molecular layer-by-layer (mLbL) technique,[24,25] followed by the construction of an overlayer consisting of submicron pillar patterns via a sol−gel based nanoimprinting method,[26] which has not been explored yet. The mLbL assembly enables the formation of the flat and uniform PA layer, which is not achievable by conventional IP, and thus subsequent creation of well-defined patterns on top of the PA layer. The hydrophilic titanium dioxide (TiO_2) pillars were uniformly patterned on the RO membrane surface in an attempt not only to investigate the antifouling effect of the unexplored complex and isotropic pattern but also to induce the synergetic antifouling effect of chemical and topographical modifications.

Water permeation measurements of the patterned RO membrane with periodic TiO_2 pillars showed significantly improved fouling resistance for both organic (Bovine Serum Albumin, BSA) and bacterial (*Pseudomonas aeruginosa, P. aeruginosa*) foulants compared to its nonpatterned counterparts. Physicochemical and structural characterization of the patterned membranes suggests that reduced contact area coupled with increased hydrophilicity by the presence of submicron hydrophilic pillars is likely to enhance fouling resistance for the large bacterial foulant. In addition, we performed computational fluid dynamics (CFD) simulation to investigate flow characteristics such as the flow profile and stress distribution near the patterned membrane surface, which is recognized as an important factor governing the fouling phenomena.[17,19] CFD results suggest that the enhanced antifouling of the patterned RO membrane for the small

DOI: 10.1021/acsami.6b10875
ACS Appl. Mater. Interfaces 2016, 8, 31433−31441

organic foulant is attributed to the enhancement in overall and local shear stress at the fluid−TiO_2 pattern interface,[17] as well as increased surface hydrophilicity.

EXPERIMENTAL SECTION

Materials. Branched polyethyleneimine (PEI, M_w = 750 000 g mol^{-1}), poly(acrylic acid) (PAA, M_w = 100,000 g mol^{-1}), *m*-phenylenediamine (MPD), trimesoyl chloride (TMC), titanium(IV) butoxide, acetylacetone, acetic acid, and phosphate buffered saline (PBS) were obtained from Sigma-Aldrich (St. Louis, MO). Sodium hydroxide (NaOH) and sodium chloride (NaCl) were purchased from Samchun Chemical (Seoul, Korea) and Junsei Chemical (Tokyo, Japan), respectively. Toluene, acetone, *n*-hexane, and 2-propanol were obtained from J.T. Baker (Avantor, Center Valley, PA). Bovine serum albumin (BSA) was purchased from Merck Millipore (Darmstadt, Germany). Difco lysogeny broth (LB) was obtained from Becton Dickinson (Franklin Lakes, NJ). Deionized (DI) water (18.2 Ω) was prepared in a Millipore Milli-Q purification system. Polyacrylonitrile (PAN) ultrafiltration membrane (PAN50, ∼180 μm in thickness) with a polyester nonwoven as a support was purchased from Nanostone Water (Eden Prairie, MN). *Pseudomonas aeruginosa* (*P. aeruginosa*, KCTC 2004) was obtained from Korean Collection for Type Cultures (Daejeon, Korea).

Membrane Preparation. A flat polyamide reverse osmosis (PA RO) membrane was prepared via the mLbL approach by following the protocol reported in our previous paper.[24,25] Briefly, first, a polyelectrolyte bilayer was coated on the hydrolyzed PAN support (HPAN, hydrolysis in 1.5 M NaOH aqueous solution at 45 °C for 2 h) via alternative electrostatic deposition of oppositely charged polyelectrolytes. The HPAN support was soaked into the cationic PEI (0.1 wt %) aqueous solution (0.5 M NaCl, pH = 10.6) for 15 min, and washed twice with DI water. Then, the membrane was dipped into the anionic PAA (0.1 wt %) aqueous solution (0.5 M NaCl, pH = 3.5) for 10 min, followed by rinsing with DI water. The thickness of this PEI/PAA bilayer was estimated to be ∼10 nm in our previous report.[25] Next, the PA selective layer was prepared by the sequential depositions of MPD and TMC monomers. The PEI/PAA-coated membrane was first dipped into MPD (1.0 wt %) solution in toluene for 30 s and rinsed with acetone. Then, the membrane was immersed into TMC (1.0 wt %) solution in toluene for 30 s and rinsed with toluene. These steps were repeated 10 times, and then the prepared membrane was dried at 70 °C for 2 min. The thickness of the PA layer prepared with 10 mLbL deposition cycles was estimated to be ∼10 nm in our previous work.[25]

Pattern Formation. The submicron TiO_2 pillar patterns were created on the flat mLbL-assembled PA membrane via a sol−gel based nanoimprinting technique (Figure 1a).[26] A 10 g portion of titanium butoxide was mixed with 6.8 g of acetylacetone, and stirred for 15 min to prepare TiO_2 sol. Then, 8 mL of 2-propanol was added into the mixture, followed by dropwise addition of 0.25 g of glacial acetic acid. The solution mixture was stirred for 1 h, and subsequently filtered by a 0.45 μm Nylon syringe filter (Acrodisc, Pall Gelman Laboratory, MI). To fabricate TiO_2 nanopatterns, the synthesized TiO_2 solution was spread on the negatively patterned polyurethane (PU) mold with the hexagonally arrayed holes. Then, the mLbL membrane was placed on top of it with the PA selective layer contacting with TiO_2 solution, and a rubber roller was gently rubbed to remove the excess TiO_2 solution and ensure uniform contact. The imprinting process was performed by annealing the sample at an optimum condition (pressure = 4 bar, temperature = 60 °C, gelation time = 30 min; see the Supporting Information S1). Then, the PU mold was carefully peeled off to obtain the TiO_2-patterned membrane. A flat TiO_2 layer was also coated on the mLbL membrane as a control for comparison with the TiO_2-patterned one. The aforementioned sol−gel imprinting protocol was employed to fabricate the TiO_2-flat membrane using an unpatterned, flat PU mold.

Membrane Characterization. The membrane morphology was characterized by atomic force microscopy (AFM, Veeco Nanoscope V) and scanning electron microscopy (SEM, FEI Inspect F50). The membrane surface AFM image of 2 μm × 2 μm was obtained in a tapping mode. SEM micrographs of the membrane surfaces and cross sections were obtained at an accelerating voltage of 10 kV. The chemical properties of the prepared TiO_2 patterns were characterized by Fourier transform infrared spectroscopy (FT-IR) and X-ray photoelectron spectroscopy (XPS). FT-IR data were collected on a Nicolet IS10 spectrometer (ThermoFischer Scientific) equipped with an attenuated total reflectance (ATR) unit. XPS spectra were recorded on a PHI-5000 Versaprobe spectrometer (ULVAC-PHI) using monochromatized Al−Kα radiation at 1.49 keV. X-ray diffraction analysis (XRD) was performed on a D/MAX 2500 X-ray diffractometer (Rigaku) with a Cu−Kα source (λ = 1.541 Å) to characterize the structural properties of the TiO_2 patterns. The diffractograms were scanned in the 2θ range from 10° to 60° at a scan rate of 2° min^{-1}. Water contact angles of the membranes were measured by the sessile drop method using a contact angle measurement system (Pheonix-300, SEO Corporation) equipped with a video capture apparatus. The surface zeta potentials of the membranes were determined with an electrophoretic measurement system (ELSZ-2000, Otsuka Electronics) using a plate sample cell. The measurement was performed using a background NaCl (10 mM) aqueous solution containing mobility-monitoring particles at pH 5.8. At least six measurements were executed to obtain the averaged values of water contact angle and surface zeta potential. Membrane performance was evaluated by filtrating NaCl (2000 mg L^{-1}) aqueous solution at pH 5.8 through the membrane having an effective area (A) of 0.79 cm^2 in a cross-flow filtration system. Details about the filtration equipment and membrane cell module are described in the Supporting Information S2. Filtration test was conducted at an operating pressure of 15.5 bar and temperature of 25 °C with a flow rate of 1 L min^{-1}. Before data collection, membranes were precompacted for 24 h until their water flux reached a steady-state value. The water flux (J_w, L m^2 h^{-1}) was determined from the amount of the collected permeate (V) for a fixed time (t, typically ∼ 1 h) as given by $J_w = V/At$. Salt rejection (R, %) was calculated from the salt concentrations of the feed (C_f) and permeate (C_p) measured with an Ultrameter II conductivity meter (Myron L. Company) by using the equation, $R = 100 \times (1 - C_p/C_f)$. Performance values were obtained by averaging at least three measurements.

Membrane Fouling. Membrane fouling was assessed by monitoring the change in permeate flux after the addition of model foulants (BSA and *P. aeruginosa* as model organic and bacteria foulants, respectively) during cross-flow filtration. For the organic fouling test, membranes were stabilized with DI water at an operating pressure of 15.5 bar with a flow rate of 1 L min^{-1} to reach the steady-state condition. Then, BSA was added to the feed reservoir to make the feed BSA concentration of 100 mg L^{-1} and the permeate flux was collected at certain time intervals. For the bacteria fouling test, a bacteria stock solution was prepared prior to the experiment. The *P. aeruginosa* was grown overnight at 37 °C in LB media with shaking. The prepared bacteria solution was diluted in fresh LB broth, followed by incubation for 3 h. The bacteria culture was centrifuged at 13 500 rpm for 1 min, and the separated bacteria were redispersed in a PBS (10 mM) solution at pH 7.4 to prepare a bacteria stock solution. The stock solution was diluted to the 10^6 colony forming units (CFU) mL^{-1}. Membranes were stabilized by filtrating the broth with LB (100 mg L^{-1}) and PBS (2 mM) at 15.5 bar. After the flux reached a steady state, the bacteria suspension was added to the broth at a ratio of 1:1000 to adjust the bacteria concentration of the feed solution to 10^3 CFU mL^{-1}. Then, the permeate flux was monitored and the extent of the membrane fouling was evaluated by the relative flux, which is the measured flux normalized by the initial value. Three measurements were conducted to obtain the averaged relative flux values.

CFD Simulation. Three-dimensional numerical simulation for steady Navier−Stokes flows in the vicinity of the membrane surface was carried out using the COMSOL solver to theoretically interpret fouling behavior for the TiO_2-flat and TiO_2-patterned membranes.[17] On the basis of the finite element method, governing equations of an incompressible Newtonian fluid were solved with the combination of proper boundary conditions in the computational domains. Shear

DOI: 10.1021/acsami.6b10875
ACS Appl. Mater. Interfaces 2016, 8, 31433−31441

stress distribution on the membrane surface was evaluated from the velocity profiles. Detailed computation procedure can be found in the Supporting Information S3.

RESULTS AND DISCUSSION

Membrane Fabrication. TiO_2 was selected as a pattern material as it has been shown to be hydrophilic and favorable for retarding foulant attachment, which we envision to provide a synergistic combination of surface chemistry and topography for antifouling function. As illustrated in Figure 1a, our approach involves patterning a TiO_2 nanopillar pattern overlayer onto the surface of the molecular layer-by-layer (mLbL) assembled, flat PA RO membrane via a sol−gel nanoimprinting technique. Unlike other possible strategies that directly modify the structure of the selective layer or the support, our approach was selected to ensure robust pattern formation without affecting the RO selective layer and the underlying porous support, thus minimizing the degradation of the water desalinating performance.

AFM and SEM confirm that the neat mLbL PA membrane (Figure 1b−d), which was originally smooth, was decorated with a hexagonal array of cylindrical TiO_2 pillars with diameter, height, and spacing of 140, 160, and 400 nm, respectively (Figure 1e−g). The arithmetic average (R_a) and root-mean-square (*rms*) roughness values estimated from AFM were 5.0 ± 0.3 nm and 7.1 ± 0.5 nm, respectively, for the neat mLbL PA membrane and 56.8 ± 3.6 nm and 61.7 ± 4.1 nm, respectively, for the TiO_2-patterned membrane. FT-IR spectra of the neat mLbL membrane confirm the fully aromatic PA chemistry prepared with MPD and TMC (see the Supporting Information S4).[25] XRD results showed that the characteristic 2θ peaks of TiO_2 appeared at 24° and 37°, corresponding to [101] and [004] planes, respectively (see the Supporting Information S5).[27] The weak and broad XRD diffraction pattern indicates relatively low crystallinity of the TiO_2, presumably due to the high amount of the precursor residue, titanium butoxide. The low crystallinity of TiO_2 would enable permeation of water molecules through the amorphous regions of the TiO_2 layer. This residual precursor is known to undergo hydrolysis upon exposure to water,[28] thus possibly altering the physicochemical properties of the TiO_2-patterned membranes in an aqueous media.

To confirm this, we studied the chemical properties of TiO_2-patterned membranes before and after water permeation tests using FT-IR and XPS. FT-IR spectra of the TiO_2-patterned membrane show that two characteristic peaks of Ti−O−Ti bonds (900−400 cm^{-1})[29,30] become pronounced after the water permeation test (Figure 2a), although adsorbed water could result in the variation in the background spectra to some extent.[31] More detailed discussion on the analysis of FT-IR spectra is provided in the Supporting Information S6. In order to further confirm the possible TiO_2 hydrolysis, we performed XPS analysis. Consistently, high-resolution O 1s XPS spectra (Figure 2b) reveal that the peak at 530.1 eV (Ti−O−Ti) becomes more pronounced and a new peak develops at 531.7 eV (Ti−O−H) while the peak at 532.4 eV (C−O of unhydrolyzed precursor) becomes suppressed after the water permeation test (see the Supporting Information S7).[32,33] These results suggest the formation of Ti−OH and Ti−O−Ti bonds by hydrolysis and subsequent condensation reaction, respectively, of the remaining precursors within the TiO_2 layer during the water permeation test. Hydrolysis of the incipient TiO_2 layer also leads to a change in its affinity with water, which

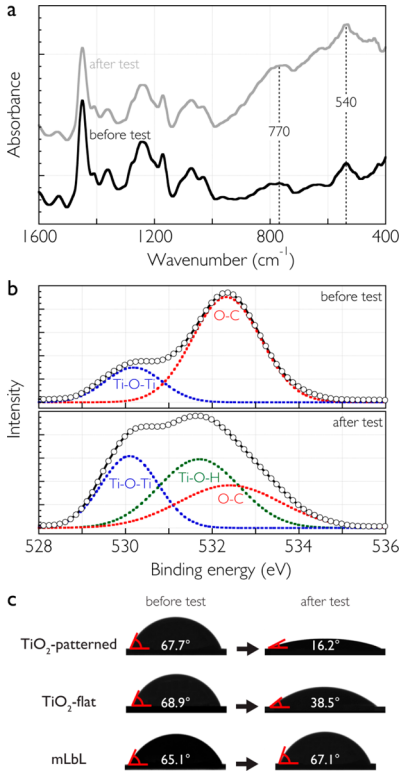

Figure 2. (a) FT-IR spectra of the TiO_2-patterned membrane before and after water permeation test. (b) High-resolution O 1s XPS spectra of the TiO_2-patterned membrane before and after water permeation test. (c) Water contact angles of the neat mLbL, TiO_2-flat, and TiO_2-patterned membranes before and after water permeation test.

was demonstrated via water contact angle measurements (Figure 2c). Both the TiO_2-coated membranes showed remarkable reduction in water contact angle (from 68.9 ± 6.4° to 38.5 ± 1.9° for flat and from 67.7 ± 5.0° to 16.2 ± 2.0° for the patterned one) following the water permeation test. This is in stark contrast with the neat mLbL PA membrane, which showed no noticeable change in the water contact angle (65.1 ± 4.7° vs 67.1 ± 5.6°). This increased wettability of the TiO_2-coated membranes after water exposure is attributed to the increased number of surface −OH groups by hydrolysis, as evidenced by the above XPS result. Both the TiO_2-flat and the TiO_2-patterned membranes show the greater water wettability than the mLbL PA membrane due to the intrinsic hydrophilicity of TiO_2. This result is in good qualitative agreement with the reports by other researchers, who observed the decreased water contact angle of PA membranes after surface deposition with TiO_2 nanoparticles, which was also attributed to the great hydrophilicity of TiO_2.[34,35] To understand the effect of surface topography on the membrane wettability, we compared contact angle results between the TiO_2-flat membrane and the TiO_2-patterned membrane. The TiO_2-patterned membrane has a lower water contact angle than the TiO_2-flat membrane (16.2 ± 2.0° vs 38.5 ± 1.9°). This result can be explained by the Wenzel model that predicts the enhanced wettability by increasing roughness for hydrophilic materials including TiO_2.[36] The TiO_2 layer coating on the mLbL membrane also significantly alters the surface charge properties. The neat mLbL PA membrane surface exhibited the negative surface zeta potential value of −27.6 ± 1.9 mV under the operating pH of 5.8. TiO_2 coating leads to an increase in

DOI: 10.1021/acsami.6b10875
ACS Appl. Mater. Interfaces 2016, 8, 31433−31441

the surface zeta potential value, suggesting that the density of negatively charged groups on the membrane surface is reduced by the TiO_2 coating: The surface zeta potential is estimated to be 4.8 ± 0.4 mV and −3.2 ± 0.4 mV for the TiO_2-flat and TiO_2-patterned membranes, respectively.[37] This result is also qualitatively supported by Lee et al's work where TiO_2 nanoparticles were used as positively charged building blocks to compensate the negative charge of the counterpart building blocks for the electrostatic interaction-induced layer-by-layer assembly.[38]

Membrane Performance and Stability. Figure 3a shows the water flux and NaCl rejection of the neat mLbL and TiO_2-patterned membranes. Both membranes exhibited NaCl rejection required for RO applications. Specifically, the neat mLbL membrane has a water flux of 29.5 ± 3.1 L m^{-2} h^{-1} and NaCl rejection of 97.7 ± 1.3%. Compared to the neat mLbL membrane, the TiO_2-patterned membrane exhibited a lower water flux, 10.8 ± 1.9 L m^{-2} h^{-1}, but higher NaCl rejection, 98.3 ± 0.8%. This reduction in water flux is attributed to the increased hydrodynamic resistance by the patterned TiO_2 layer. In fact, membrane surface coating strategies to enhance antifouling often led to an inevitable reduction in water permeability. For example, Louie et al. reported the maximum ~75% water flux decline of the RO membrane after surface coating with the polyether−polyamide block copolymer as a antifouling material.[39] It should be noted that the flux decline rate of our patterned membrane could be controlled by rationally designing pattern geometry such as basal layer thickness. The increase in NaCl rejection is likely due to the reduction of local defects on the mLbL surface by the TiO_2 layer, which is consistent with the report that the membrane salt rejection can be enhanced by plugging the local defects with a coating.[40] This rejection enhancement could somewhat compensate the disadvantageous flux loss by TiO_2 patterning.

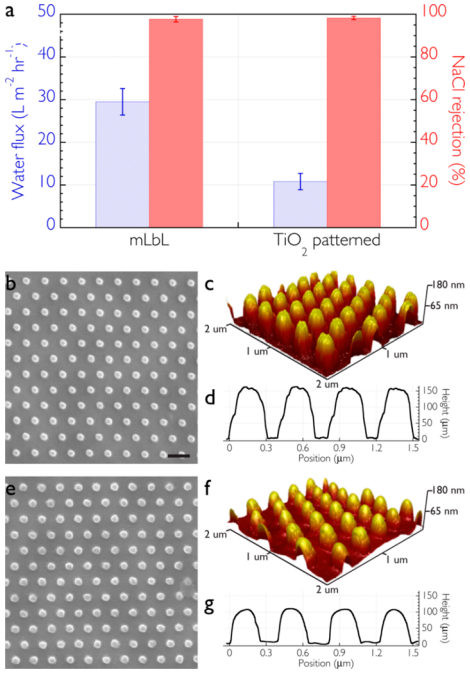

Figure 3. (a) Water flux and NaCl rejection of the neat mLbL and TiO_2-patterned membranes. (b−d) Top-down SEM, AFM, and AFM height profiles of the TiO_2-patterned membrane before permeation test. (e−g) Top-down SEM, AFM, and AFM height profiles of the TiO_2-patterned membrane after permeation test. Scale bar = 500 nm for SEM images.

Besides short-term membrane performance, pattern stability is critical to maintaining the antifouling properties over the course of the membrane lifetime. We evaluated the TiO_2 pattern stability by comparing the change in the TiO_2 pillar morphology using SEM and AFM before and after a 24 h water permeation test (Figure 3b−g). Neither breakage nor delamination of the pillars was visible, demonstrating the robustness of the patterns. However, AFM results revealed a height reduction of the pillars from ~160 to ~120 nm as well as a volume reduction (Figure 3c,d and f,g). It was also found from AFM results that R_a and *rms* roughness values were reduced to 41.4 ± 2.9 nm and 48.8 ± 3.4 nm, respectively, from 56.8 ± 3.6 nm and 61.7 ± 4.1 nm, respectively. We speculate that this shrinkage is attributed partially to metal oxide formation via hydrolytic condensation reaction of the residual alkoxide precursors that remained in the TiO_2 upon water exposure, as evidenced by the chemical analysis results.[41] Since the bottom side of the patterns is constrained on the surface, the pattern shrinkage is more pronounced for the height direction rather than the lateral direction.[42]

Membrane Fouling. Figure 4 shows the change in the water flux as a function of filtration time of the three membrane systems upon the addition of model organic (BSA, Figure 4a)

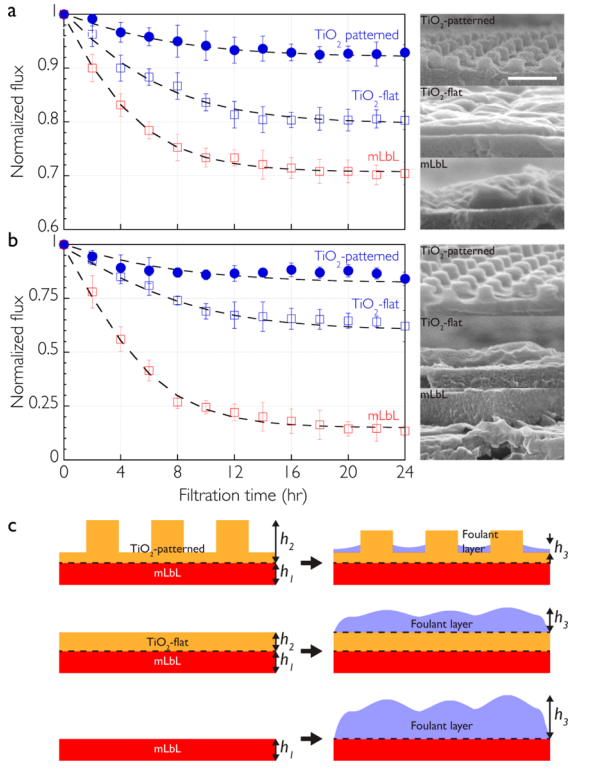

Figure 4. Fouling test of the three membrane materials. (a) Normalized water flux of the neat mLbL, TiO_2-flat, and TiO_2-patterned membranes as a function of filtration time with the addition of BSA. The SEM images show cross sections of three membranes after the fouling test. Scale bar = 500 nm. (b) Normalized water flux of the neat mLbL, TiO_2-flat, and TiO_2-patterned membranes as a function of filtration time with the addition of *P. aeruginosa*. The SEM images show cross sections of three membranes after the fouling test. (c) Schematic representation of the accumulation of the foulant layer for the three membrane surfaces with filtration time.

DOI: 10.1021/acsami.6b10875
ACS Appl. Mater. Interfaces 2016, 8, 31433−31441

and bacterial (*P. aeruginosa*, Figure 4b) foulants. In general, the TiO_2-coated membranes have significantly better antifouling resistance compared to the neat mLbL membrane regardless of the type of foulant. In the case of the BSA study, the decline of the water flux for the mLbL membrane was quite drastic and led to a water flux reduction of ~30% (Figure 4a). On the other hand, the extent of water flux reduction for both the TiO_2-flat membrane (~20%) and TiO_2-patterned membrane (~8%) was significantly lower than that of the mLbL membrane. It is important to note that the TiO_2-patterned membrane demonstrated a lower water flux decline compared with the TiO_2-flat membrane, which suggests that surface chemistry and topography synergistically yields significantly enhanced antifouling properties. Weinman et al. also observed that the combination of physical patterning and hydrophilic chemical coating on the membrane resulted in the better organic antifouling than either method alone.[43] Fouling tendency was confirmed by the cross-sectional SEM images of the fouled membranes showing that the neat mLbL membrane has the thickest organic foulant layer (~250 nm), followed by the TiO_2-flat (~100 nm) and TiO_2-patterned membranes (inset of Figure 4a). It should be noted that the pattern shape of the TiO_2-patterned membrane is nearly preserved, suggesting that the fouling is likely to occur predominantly on the bottom side between the pillar patterns. Considering the original pattern height (~120 nm), the organic foulant layer thickness is estimated to be no more than 50 nm.

Biofouling by *P. aeruginosa* showed similar trends with the BSA fouling results. The neat mLbL membrane showed the largest flux decline (~90%), followed by the TiO_2-flat membrane (~40%), and the TiO_2-patterned membrane exhibited the lowest flux decline (~15%) (Figure 4b). The significant flux decline for the mLbL membrane was confirmed by the SEM cross section of the fouled membrane showing the formation of a thick (~360 nm) biofilm layer (inset of Figure 4b). Similarly, the SEM cross section of the TiO_2-flat membrane also showed the formation of a biofilm layer (~200 nm). Importantly, we observed no apparent biofilm formation for the TiO_2-patterned membrane (inset of Figure 4b), with the exception of sparsely distributed bacteria being adhered on the patterned surface (see the Supporting Information S8), demonstrating the superior biofouling resistance of the TiO_2-patterned membrane.

Regardless of the specific foulant, the water flux decline can be described as the formation and growth of a foulant layer (h_3) that increases the hydraulic resistance of the membrane (Figure 4c). As a first order approximation, we assume that the foulant grows with time with a constant growth rate (r)[44] and this layer eventually reaches a long-time limit ($h_3(\infty)$)

$$\frac{d}{dt}h_3(t) = rh_3(t)\cdot\left(1 - \frac{h_3(t)}{h_3(\infty)}\right) \tag{1}$$

The water flux decline is described as a normalized flux, $J(t)/J(0)$, which is defined as the ratio of the flux at t versus the flux at $t = 0$. For the membranes illustrated in Figure 4c, this expression is the sum of hydraulic resistance of the membrane layers[25]

$$\frac{J_w(t)}{J_w(0)} = \frac{[A_1(t)^{-1} + A_2(t)^{-1} + A_3(t)^{-1}]^{-1}}{[A_1(0)^{-1} + A_2(0)^{-1} + A_3(0)^{-1}]^{-1}} \tag{2}$$

where $A_1(t)^{-1}$, $A_2(t)^{-1}$, $A_3(t)^{-1}$ correspond to the hydraulic resistance of the mLbL layer, the TiO_2 layer, and the foulant layer at time t, respectively. The hydraulic resistance is proportional to the layer thickness; thus

$$A_1(t) = \frac{a_1}{h_1(t)}$$
$$A_2(t) = \frac{a_2}{h_2(t)}$$
$$A_3(t) = \frac{a_3}{h_3(t)} \tag{3}$$

where the constants a_1, a_2, a_3 are the water permeability coefficients of the membrane layers. Since the thickness of the mLbL and TiO_2 layers remains constant with filtration time, eq 3 can be simplified to $A_m(t)^{-1} = A_1(t)^{-1} + A_2(t)^{-1}$. Substituting eqs 1 and 3 into eq 2

$$\frac{J_w(t)}{J_w(0)} = \frac{[A_m(t)^{-1} + A_3(t)^{-1}]^{-1}}{[A_m(0)^{-1} + A_3(0)^{-1}]^{-1}} = \frac{m_1}{1 + m_2e^{rt}/1 + m_3e^{rt}} \tag{4}$$

where the coefficients, m_1, m_2, m_3 are constants that reflect the transport properties of the membrane of interest. We apply eq 4 to describe the fouling results in Figure 4 to provide a semiquantitative assessment of the growth rate of the foulant layer for three membrane systems. Table 1, which summarizes the growth rates of the foulant layers for all three membrane systems, shows that the TiO_2-patterned membrane significantly inhibited the rate of growth of the foulant layer (~0.175 h^{-1}) when compared with the neat mLbL membrane (~0.3 h^{-1}) and this behavior is nearly independent of the foulant type.

Table 1. Growth Rate of BSA and *P. aeruginosa* Foulant Layers for the Three Membrane Systems Based on Fitting eq 4 to the Results in Figure 4

foulant type	mLbL [h^{-1}]	TiO_2-flat [h^{-1}]	TiO_2-patterned [h^{-1}]
BSA	0.28	0.20	0.17
P. aeruginosa	0.30	0.19	0.16

We attribute the enhanced fouling resistance of the TiO_2-flat membrane compared with the neat mLbL membrane for both BSA and bacteria foulants, characterized as hydrophobic and negatively charged matters, to the increased hydrophilicity by the TiO_2 layer. This reduces the hydrophobic attraction between the foulant and the TiO_2-flat membrane surface, thus mitigating foulant attachment.[25] Kim et al. also claimed that the reduced organic fouling on the PA membrane coated with TiO_2 nanoparticles is attributed to the improved surface hydrophilicity imparted by the presence of TiO_2.[34] Importantly, our observation that the TiO_2-patterned membrane has better antifouling property compared to the TiO_2-flat membrane in spite of identical surface chemistry strongly suggests that topography plays a significant role in preventing foulant accumulation. It is generally accepted that the extent of fouling depends on the relative scale of the topographical feature to the dimensions of the foulant.[10] For example, topographical features whose scale is larger than the foulant can actually exacerbate fouling by providing more surface area available for foulant attachment.[10,45]

Interestingly, fouling by BSA whose dimensions are much smaller than that of the TiO_2 pattern was largely suppressed

DOI: 10.1021/acsami.6b10875
ACS Appl. Mater. Interfaces 2016, 8, 31433−31441

compared to the TiO_2-flat membrane, as we expected the rougher surface to have the opposite effect.[45] Recent studies have claimed that surface patterns can alter the local hydrodynamics in the vicinity of the pattern feature, thus inducing local turbulence and higher shear stress, ultimately leading to the suppression in foulant attachment.[16,17,21,46] It has also been experimentally demonstrated that submicron patterns on ultrafiltration membranes effectively mitigate BSA fouling, presumably due to this enhanced turbulence near the topographical features.[21]

Despite such experimental observations, theoretical evidence for the antifouling mechanism of the submicron topographic features whose dimensions are larger than those of the foulant has yet to be reported. To elucidate the effect of submicron roughness on BSA fouling, we performed three-dimensional CFD simulations[17] in order to depict the local hydrodynamic flow and shear stress distribution in the vicinity of the surface for the TiO_2-patterned and TiO_2-flat membranes. CFD analysis revealed that the wall shear stress is heterogeneously distributed around the pillars of the TiO_2-patterned membrane surface (Figure 5a,d) while the stress profile is uniform over the TiO_2-flat membrane surface (Figure 5b). To determine the average local wall shear stress (Figure 5c), we stratified the pillar into five (I–V) separate sections (Figure 5d), which show that local wall shear stress of the lower region (I–II) of the pillar is slightly lower than that of the flat membrane, thus leading to favorable BSA deposition near the bottom of the pillars (Figures 4a and 5d, inset). However, the upper region (III–V) of the pillar exhibited greater wall shear stress than that of the TiO_2-flat membrane. The top surface of the pillar drastically increases the hydrodynamic flow strength and induces approximately 5 times higher wall shear stress compared to the flat counterpart. This effect can significantly facilitate detachment and inhibit attachment of BSA near the top surface of the pattern.[16,17] This local stress distribution near the pillar is qualitatively confirmed by the cross-sectional image of the fouled TiO_2-patterned membrane where BSA is accumulated preferentially in the lower regions of the pattern, whereas the upper regions of the pillar remain nearly uncoated by the BSA (Figures 4a and 5d, inset). This result is qualitatively similar to the report by Lee et al., who observed that microbial foulants were accumulated mainly in the lower region of the microscale prism pattern on the MF membrane surface and explained this phenomenon by large suppression of local wall shear stress in this region with an aid of CFD simulation.[17] Unlike Lee et al's work where the overall wall shear stress averaged over the entire surface of the patterned membrane was smaller than that of the flat membrane, we observed that the overall wall shear stress was higher for the TiO_2-patterned membrane than the TiO_2-flat membrane (141.2 Pa vs 116.0 Pa). This indicates that our patterned membrane would more effectively mitigate fouling compared to that fabricated by Lee and co-workers. Together with increased overall wall shear stress, the local enhancement in wall shear stress is expected to improve the fouling resistance for the submicron TiO_2-patterned membrane compared to the TiO_2-flat membrane.[16,17,21]

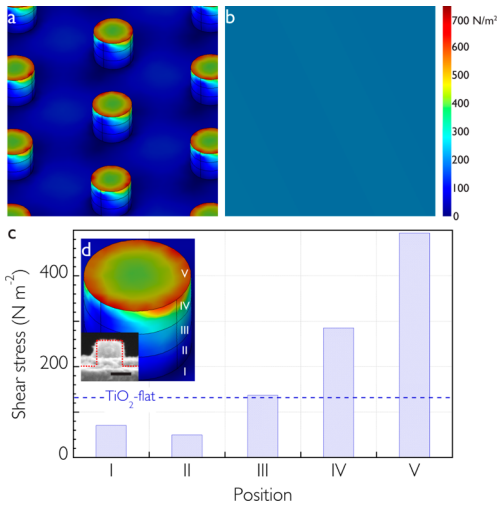

Figure 5. (a, b) Contour of the shear stress in the vicinity of the TiO_2-patterned and TiO_2-flat membrane surfaces. (c) Local wall shear stress values as a function of (d) the vertical position of the pillar pattern. The inset SEM micrograph shows the cross section of the pillar after fouling test (Scale bar = 100 nm). The dashed line denotes the value of averaged overall wall shear stress of the TiO_2-flat membrane.

In addition to higher overall and/or local wall shear stress, the pillar pattern can suppress fouling by minimizing the number of contact points and contact area of the foulant on the surface when its feature size is smaller than the foulant size.[10,12] Since the dimensions of *P. aeruginosa* (~1 μm in width and ~2 μm in length)[47] are significantly larger than those of the nanoscale TiO_2 pillar, the TiO_2-patterned membrane is believed to have better biofouling resistance than its flat counterpart by reducing the contact area for bacteria attachment. This concept is supported by Xu et al., who reported that the submicron pillar patterns on polyurethane urea films greatly limited bacterial adhesion and biofilm formation compared to the smooth controls, which was attributed to the reduction in area available for bacterial contact.[12] Furthermore, Kwak et al. reported that the TiO_2 nanoparticle-coated PA membrane had a slight, but distinct, photocatalysis effect on bacteria even in a dark environment. Hence, the potential photocatalytic bactericidal capability of TiO_2 could possibly contribute to biofouling reduction, although further systematic study is needed to verify this effect.[48]

CONCLUSIONS

We have successfully fabricated an RO membrane patterned with periodic, submicron TiO_2 pillars using a combination of the sol–gel nanoimpriting and the mLbL assembly methods. The TiO_2-patterned membrane shows improved antifouling resistance to both organic (BSA) and bacterial (*P. aeruginosa*) foulants due to the synergetic effect of surface chemistry and topography. The presence of a hydrophilic TiO_2 layer generally suppresses attachment of the hydrophobic foulants on the membrane surface by reducing hydrophobic attraction. The nanoscale TiO_2 pillar pattern further enhances antifouling performance, depending on the relative foulant size, by reducing the contact area for microscale bacteria attachment or by enhancing local shear stress for molecular-scale BSA adhesion. Our proposed fabrication strategy presents new opportunities for designing functional membranes and surfaces having antifouling, anti-adhesion, and self-cleaning abilities while also providing a model platform for elucidating the antifouling mechanism.

ASSOCIATED CONTENT

Supporting Information

The Supporting Information is available free of charge on the ACS Publications website at DOI: 10.1021/acsami.6b10875.

DOI: 10.1021/acsami.6b10875
ACS Appl. Mater. Interfaces 2016, 8, 31433–31441

SEM micrographs of the TiO_2 patterns prepared with various gelation conditions, Schematic of the filtration equipment, FT-IR spectra of membranes, detailed CFD simulation procedure, XRD spectrum of the TiO_2 pattern, and SEM micrograph of the TiO_2-patterned membrane surface fouled by *P. aeruginosa* (PDF)

AUTHOR INFORMATION

Corresponding Authors

*E-mail: dhko@khu.ac.kr. Phone: +82-31-201-3844. Fax: +82-31-201-3855 (D.-H.K.).

*E-mail: leejhyyy@korea.ac.kr. Phone: +82-2-3290-3293. Fax: +82-2-926-6102 (J.-H.L.).

Author Contributions

[∇]The manuscript was written through contributions of all authors. All authors have given approval to the final version of the manuscript. These authors contributed equally.

Notes

The authors declare no competing financial interest.

ACKNOWLEDGMENTS

This research was supported by the Basic Science Research Program through the National Research Foundation of Korea (NRF) funded by the Ministry of Science, ICT & Future Planning (NRF-2016M3C1A3909138) and by the Fundamental R&D Program for Technology of World Premier Materials funded by the Ministry of Trade, Industry and Energy, Republic of Korea (10037794), and by Korea Ministry of Environment as "Global Top Project (2016002100007)".

REFERENCES

(1) An, Q. F.; Li, F.; Ji, Y. L.; Chen, H. L. Influence of Polyvinyl Alcohol on the Surface Morphology, Separation and Anti-fouling Performance of the Composite Polyamide Nanofiltration Membranes. *J. Membr. Sci.* **2011**, *367*, 158−165.

(2) Bano, S.; Mahmood, A.; Kim, S. J.; Lee, K. H. Graphene Oxide Modified Polyamide Nanofiltration Membrane with Improved Flux and Antifouling Properties. *J. Mater. Chem. A* **2015**, *3*, 2065−2071.

(3) Ji, Y. L.; An, Q. F.; Guo, Y. S.; Hung, W. S.; Lee, K. R.; Gao, C. J. Bio-inspired Fabrication of High Perm-selectivity and Anti-fouling Membranes Based on Zwitterionic Polyelectrolyte Nanoparticles. *J. Mater. Chem. A* **2016**, *4*, 4224−4231.

(4) Liu, L. F.; Yu, S. C.; Wu, L. G.; Gao, C. H. Study on a Novel Polyamide-urea Reverse Osmosis Composite Membrane (ICIC-MPD) II. Analysis of Membrane Antifouling Performance. *J. Membr. Sci.* **2006**, *283*, 133−146.

(5) Kang, G. D.; Cao, Y. M. Development of Antifouling Reverse Osmosis Membranes for Water Treatment: A Review. *Water Res.* **2012**, *46*, 584−600.

(6) Kang, G. D.; Liu, M.; Lin, B.; Cao, Y. M.; Yuan, Q. A Novel Method of Surface Modification on Thin-film Composite Reverse Osmosis Membrane by Grafting Poly(ethylene glycol). *Polymer* **2007**, *48*, 1165−1170.

(7) Mansouri, J.; Harrisson, S.; Chen, V. Strategies for Controlling Biofouling in Membrane Filtration Systems: Challenges and Opportunities. *J. Mater. Chem.* **2010**, *20*, 4567−4586.

(8) Hasan, J.; Chatterjee, K. Recent Advances in Engineering Topography Mediated Antibacterial Surfaces. *Nanoscale* **2015**, *7*, 15568−15575.

(9) Carman, M. L.; Estes, T. G.; Feinberg, A. W.; Schumacher, J. F.; Wilkerson, W.; Wilson, L. H.; Callow, M. E.; Callow, J. A.; Brennan, A. B. Engineered Antifouling Microtopographies - Correlating Wettability with Cell Attachment. *Biofouling* **2006**, *22*, 11−21.

(10) Efimenko, K.; Finlay, J.; Callow, M. E.; Callow, J. A.; Genzer, J. Development and Testing of Hierarchically Wrinkled Coatings for Marine Antifouling. *ACS Appl. Mater. Interfaces* **2009**, *1*, 1031−1040.

(11) Chung, K. K.; Schumacher, J. F.; Sampson, E. M.; Burne, R. A.; Antonelli, P. J.; Brennan, A. B. Impact of Engineered Surface Microtopography on Biofilm Formation of Staphylococcus Aureus. *Biointerphases* **2007**, *2*, 89−94.

(12) Xu, L. C.; Siedlecki, C. A. Submicron-textured Biomaterial Surface Reduces Staphylococcal Bacterial Adhesion and Biofilm Formation. *Acta Biomater.* **2012**, *8*, 72−81.

(13) Gencal, Y.; Durmaz, E. N.; Culfaz-Emecen, P. Z. Preparation of Patterned Microfiltration Membranes and Their Performance in Crossflow Yeast Filtration. *J. Membr. Sci.* **2015**, *476*, 224−233.

(14) Maruf, S. H.; Wang, L.; Greenberg, A. R.; Pellegrino, J.; Ding, Y. F. Use of Nanoimprinted Surface Patterns to Mitigate Colloidal Deposition on Ultrafiltration Membranes. *J. Membr. Sci.* **2013**, *428*, 598−607.

(15) Vogelaar, L.; Lammertink, R. G. H.; Barsema, J. N.; Nijdam, W.; Bolhuis-Versteeg, L. A. M.; van Rijn, C. J. M.; Wessling, M. Phase Separation Micromolding: A New Generic Approach for Microstructuring Various Materials. *Small* **2005**, *1*, 645−655.

(16) Won, Y. J.; Lee, J.; Choi, D. C.; Chae, H. R.; Kim, I.; Lee, C. H.; Kim, I. C. Preparation and Application of Patterned Membranes for Wastewater Treatment. *Environ. Sci. Technol.* **2012**, *46*, 11021−11027.

(17) Lee, Y. K.; Won, Y. J.; Yoo, J. H.; Ahn, K. H.; Lee, C. H. Flow Analysis and Fouling on the Patterned Membrane Surface. *J. Membr. Sci.* **2013**, *427*, 320−325.

(18) Won, Y. J.; Choi, D. C.; Jang, J. H.; Lee, J. W.; Chae, H. R.; Kim, I.; Ahn, K. H.; Lee, C. H.; Kim, I. C. Factors Affecting Pattern Fidelity and Performance of a Patterned Membrane. *J. Membr. Sci.* **2014**, *462*, 1−8.

(19) Won, Y. J.; Jung, S. Y.; Jang, J. H.; Lee, J. W.; Chae, H. R.; Choi, D. C.; Ahn, K. H.; Lee, C. H.; Park, P. K. Correlation of Membrane Fouling with Topography of Patterned Membranes for Water Treatment. *J. Membr. Sci.* **2016**, *498*, 14−19.

(20) Maruf, S. H.; Greenberg, A. R.; Pellegrino, J.; Ding, Y. F. Critical Flux of Surface-patterned Ultrafiltration Membranes during Cross-flow Filtration of Colloidal Particles. *J. Membr. Sci.* **2014**, *471*, 65−71.

(21) Maruf, S. H.; Rickman, M.; Wang, L.; Mersch, J., IV; Greenberg, A. R.; Pellegrino, J.; Ding, Y. F. Influence of Sub-micron Surface Patterns on the Deposition of Model Proteins during Active Filtration. *J. Membr. Sci.* **2013**, *444*, 420−428.

(22) Maruf, S. H.; Greenberg, A. R.; Ding, Y. F. Influence of Substrate Processing and Interfacial Polymerization Conditions on the Surface Topography and Permselective Properties of Surface-patterned Thin-film Composite Membranes. *J. Membr. Sci.* **2016**, *512*, 50−60.

(23) Maruf, S. H.; Greenberg, A. R.; Pellegrino, J.; Ding, Y. F. Fabrication and Characterization of a Surface-patterned Thin Film Composite Membrane. *J. Membr. Sci.* **2014**, *452*, 11−19.

(24) Choi, W.; Gu, J. E.; Park, S. H.; Kim, S.; Bang, J.; Baek, K. Y.; Park, B.; Lee, J. S.; Chan, E. P.; Lee, J. H. Tailor-Made Polyamide Membranes for Water Desalination. *ACS Nano* **2015**, *9*, 345−355.

(25) Gu, J. E.; Lee, S.; Stafford, C. M.; Lee, J. S.; Choi, W.; Kim, B. Y.; Baek, K. Y.; Chan, E. P.; Chung, J. Y.; Bang, J.; Lee, J. H. Molecular Layer-by-Layer Assembled Thin-Film Composite Membranes for Water Desalination. *Adv. Mater.* **2013**, *25*, 4778−4782.

(26) Hampton, M. J.; Williams, S. S.; Zhou, Z.; Nunes, J.; Ko, D. H.; Templeton, J. L.; Samulski, E. T.; DeSimone, J. M. The Patterning of Sub-500 nm Inorganic Oxide Structures. *Adv. Mater.* **2008**, *20*, 2667−2673.

(27) Guo, Y. G.; Hu, Y. S.; Sigle, W.; Maier, J. Superior Electrode Performance of Nanostructured Mesoporous TiO2 (anatase) through Efficient Hierarchical Mixed Conducting Networks. *Adv. Mater.* **2007**, *19*, 2087−2091.

(28) Honda, H.; Suzaki, K.; Sugahara, Y. Control of Hydrolysis and Condensation Reactions of Titanium Tert-butoxide by Chemical Modification with Catechol. *J. Sol-Gel Sci. Technol.* **2001**, *22*, 133−138.

(29) Mauritz, K. A.; Jones, C. K. Novel Poly(Normal-Butyl Methacrylate) Titanium-Oxide Alloys Produced by the Sol-Gel

DOI: 10.1021/acsami.6b10875
ACS Appl. Mater. Interfaces 2016, 8, 31433−31441

Process for Titanium Alkoxides. *J. Appl. Polym. Sci.* **1990**, *40*, 1401−1420.
(30) Soler-Illia, G. J. D. A.; Louis, A.; Sanchez, C. Synthesis and Characterization of Mesostructured Titania-based Materials through Evaporation-induced Self-assembly. *Chem. Mater.* **2002**, *14*, 750−759.
(31) Marechal, Y. The Molecular Structure of Liquid Water Delivered by Absorption Spectroscopy in the Whole IR Region Completed with Thermodynamics Data. *J. Mol. Struct.* **2011**, *1004*, 146−155.
(32) Yu, J. G.; Zhao, X. J.; Zhao, Q. N. Effect of Surface Structure on Photocatalytic Activity of TiO2 Thin Films Prepared by Sol-gel Method. *Thin Solid Films* **2000**, *379*, 7−14.
(33) Liu, S. H.; Zhao, Z. H.; Wang, Z. Z. Photocatalytic Reduction of Carbon Dioxide Using Sol-gel Derived Titania-supported CoPc Catalysts. *Photochem. Photobiol. Sci.* **2007**, *6*, 695−700.
(34) Kim, S. J.; Lee, P. S.; Bano, S.; Park, Y. I.; Nam, S. E.; Lee, K. H. Effective Incorporation of TiO2 Nanoparticles into Polyamide Thin-film Composite Membranes. *J. Appl. Polym. Sci.* **2016**, *133*, 43383.
(35) Zhang, R. X.; Braeken, L.; Luis, P.; Wang, X. L.; Van der Bruggen, B. Novel Binding Procedure of TiO2 Nanoparticles to Thin Film Composite Membranes via Self-polymerized Polydopamine. *J. Membr. Sci.* **2013**, *437*, 179−188.
(36) Li, Y.; Sasaki, T.; Shimizu, Y.; Koshizaki, N. A Hierarchically Ordered TiO2 Hemispherical Particle Array with Hexagonal-Non-Close-Packed Tops: Synthesis and Stable Superhydrophilicity Without UV Irradiation. *Small* **2008**, *4*, 2286−2291.
(37) Miyauchi, M.; Ikezawa, A.; Tobimatsu, H.; Irie, H.; Hashimoto, K. Zeta Potential and Photocatalytic Activity of Nitrogen Doped TiO2 Thin Films. *Phys. Chem. Chem. Phys.* **2004**, *6*, 865−870.
(38) Lee, D.; Rubner, M. F.; Cohen, R. E. All-nanoparticle Thin-film Coatings. *Nano Lett.* **2006**, *6*, 2305−2312.
(39) Louie, J. S.; Pinnau, I.; Ciobanu, I.; Ishida, K. P.; Ng, A.; Reinhard, M. Effects of Polyether-polyamide Block Copolymer Coating on Performance and Fouling of Reverse Osmosis Membranes. *J. Membr. Sci.* **2006**, *280*, 762−770.
(40) Tang, C. Y. Y.; Kwon, Y. N.; Leckie, J. O. Effect of Membrane Chemistry and Coating Layer on Physiochemical Properties of Thin Film Composite Polyamide RO and NF Membranes I. FTIR and XPS Characterization of Polyamide and Coating Layer Chemistry. *Desalination* **2009**, *242*, 149−167.
(41) Yoldas, B. E. Hydrolysis of Titanium Alkoxide and Effects of Hydrolytic Polycondensation Parameters. *J. Mater. Sci.* **1986**, *21*, 1087−1092.
(42) Richmond, D. A.; Zhang, Q.; Cao, G.; Weiss, D. N. Pressureless Nanoimprinting of Anatase TiO2 Precursor Films. *J. Vac. Sci. Technol. B* **2011**, *29*, 021603.
(43) Weinman, S. T.; Husson, S. M. Influence of Chemical Coating Combined with Nanopatterning on Alginate Fouling during Nanofiltration. *J. Membr. Sci.* **2016**, *513*, 146−154.
(44) Yang, L.; Haagensen, J. A. J.; Jelsbak, L.; Johansen, H. K.; Sternberg, C.; Hoiby, N.; Molin, S. In Situ Growth Rates and Biofilm Development of Pseudomonas Aeruginosa Populations in Chronic Lung Infections. *J. Bacteriol.* **2008**, *190*, 2767−2776.
(45) Li, Q. L.; Xu, Z. H.; Pinnau, I. Fouling of Reverse Osmosis Membranes by Biopolymers in Wastewater Secondary Effluent: Role of Membrane Surface Properties and Initial Permeate Flux. *J. Membr. Sci.* **2007**, *290*, 173−181.
(46) Gohari, R. J.; Lau, W. J.; Matsuura, T.; Ismail, A. F. Effect of Surface Pattern Formation on Membrane Fouling and Its Control in Phase Inversion Process. *J. Membr. Sci.* **2013**, *446*, 326−331.
(47) Medilanski, E.; Kaufmann, K.; Wick, L. Y.; Wanner, O.; Harms, H. Influence of the Surface Topography of Stainless Steel on Bacterial Adhesion. *Biofouling* **2002**, *18*, 193−203.
(48) Kwak, S. Y.; Kim, S. H.; Kim, S. S. Hybrid Organic/inorganic Reverse Osmosis (RO) Membrane for Bactericidal Anti-fouling. 1. Preparation and Characterization of TiO2 Nanoparticle Self-assembled Aromatic Polyamide Thin-film-composite (TFC) Membrane. *Environ. Sci. Technol.* **2001**, *35*, 2388−2394.

DOI: 10.1021/acsami.6b10875
ACS Appl. Mater. Interfaces 2016, 8, 31433−31441